

# A new code for computing differentially rotating neutron stars

Samuel D. Tootle,<sup>1,2</sup> Terrence Pierre Jacques,<sup>1,3,4</sup> and Marie Cassing<sup>2</sup>

<sup>1</sup>*Department of Physics, University of Idaho, Moscow, ID 83843, USA*

<sup>2</sup>*Institute for Theoretical Physics, Goethe University, Frankfurt, Germany*

<sup>3</sup>*Department of Physics and Astronomy, West Virginia University, Morgantown, WV 26506, USA*

<sup>4</sup>*Center for Gravitational Waves and Cosmology, West Virginia University, Chestnut Ridge Research Building, Morgantown, WV 26505*

(Dated: January 9, 2026)

We present new initial data codes for constructing stationary, axisymmetric equilibrium models of differentially rotating neutron stars in full general relativity within the Frankfurt University/KADATH (FUKA) suite of initial data codes. FUKA leverages the KADATH spectral library to solve the Einstein equations under the assumption of an isentropic fluid without magnetic fields while incorporating GRHayEOS to support 3D tabulated equations of state in *stellar collapse* format. The two solvers explored in this work include one using quasi-isotropic coordinates (QIC) in Spherical coordinates while the other solves the eXtended Conformal Thin Sandwich (XCTS) decomposition in Cartesian coordinates, enabling the construction of equilibrium configurations with high accuracy and efficiency. In this work we adopt the Komatsu-Eriguchi-Hachisu differential rotation law, however, the code is designed to be extensible to other rotation laws, allowing for exploration of physically relevant sequences and critical rotation thresholds. Furthermore, we perform convergence tests demonstrating the exponential accuracy of the spectral approach, we validate QIC and XCTS solutions against models well-studied in the literature, and we also compare FUKA solutions against the well-known RNS code. Finally, we explore the impact that initial data resolution has on dynamical simulations and recover the convergence order of the evolution scheme, the dominate source of error in this study. The new FUKA codes and results presented here lay the foundation for future extensions to more general configurations, including magnetic fields, removal of isentropic assumptions, and binary systems, and have been made publicly available to support community efforts in modeling differentially rotating relativistic stars.

## I. INTRODUCTION

Gravitational-wave astronomy, particularly when combined with electromagnetic observations, has transformed our ability to probe the dynamics and micro-physics of compact stellar objects [1–4]. Many astrophysical scenarios, such as core-collapse supernovae [5, 6], accretion-induced collapse [7, 8], and binary neutron-star (BNS) mergers [9–11], can lead to the formation of hot, rapidly and differentially rotating remnants [12–16]. These remnants can encounter non-axisymmetric instabilities, motivating the critical need for accurate equilibrium models and diagnostics that connect quasi-equilibrium sequences to dynamical behavior [17–20]. However, developing accurate models for these systems requires high-accuracy numerical relativity (NR) simulations capable of capturing dynamics that span several length and time scales. The first step towards enabling accurate and efficient studies of systems in these unique configurations is the calculation of initial data solutions that satisfy the general relativistic constraint equations, the focus of this work.

A computationally less costly approach to studying rotating stars is to assume uniform rotation. Previous studies of rotating equilibria have shown the existence of (i) a Keplerian stability line, beyond which mass shedding takes place, and (ii) the existence of a turning-point stability line. While (ii) is an indication of an unstable solution, it is not necessarily a sufficient condition for

the onset of a dynamical instability that will eventually lead to gravitational collapse [21, 22]. More importantly, the maximum mass allowed by uniform rotation and the maximum mass of the corresponding non-rotating configuration show a proportionality and even universal relation [23–26].

Constructing stationary, axisymmetric equilibria with differential rotation requires closing the relativistic Euler integral with a rotation law. The Komatsu–Eriguchi–Hachisu (KEH) prescription [27]—often termed the  $j$ -constant law—has long served as the baseline for modeling differential rotation because of its computational simplicity and the existence of an analytic solution to the first integral of motion. In addition to providing valuable insight into the impact of differential rotation on stellar structure and stability, the KEH model serves as a test bed for new initial data codes to validate their implementation. This includes a wide array of public initial data codes such as RNS [28], XNS<sup>1</sup> [29, 30], and LORENE [31] as well as private initial data codes such as COCAL [32]. Public initial data codes have played an essential role in enabling systematic studies of differentially rotating sequences, stellar equilibrium properties [30, 33–45] and their dynamical behavior [39, 46–48]. At the same time, sustained progress has broadened the rotation-law landscape. Motivated by profiles extracted

---

<sup>1</sup> Support for cold tabulated EOS has become available in XNSv4

from merger simulations, where the angular velocity often peaks off-axis, generalized prescriptions that specify  $\Omega(j)$  rather than  $j(\Omega)$  have been introduced and explored in detail, including the multi-parameter families proposed by Uryu+ [32] and subsequent variants [see e.g., 20, 49–51]. Such laws allow for better control over core and envelope regions and facilitate targeted comparisons to merger-inspired equilibria [52].

Contributions to the public initial data code landscape are essential to validate the accuracy of previous results, provide additional support for models with predictive power, and enable the broader community to participate in novel exploration. In this spirit, this work aims to contribute to this rich community and to chart a path towards areas of advancements to broaden our ability to explore astrophysical systems of interest involving differentially rotating neutron stars, using the Frankfurt University/KADATH (FUKA) initial-data framework.

FUKA is a suite of multi-purpose, multi-physics initial data (ID) solvers that leverage spectral methods to solve the Einstein constraint equations for a variety of astrophysical scenarios. FUKA is built on the KADATH spectral library [53] and has been utilized to compute initial data for highly mass-asymmetric and spinning binary black holes (BBH), binary neutron stars (BNS), and black hole-neutron star binaries [54]. FUKA has been instrumental in reliably exploring extreme regions of the space of parameters for BNS and BHNS configurations, enabled by its robust solving framework, high accuracy, and support for piecewise polytropic and cold tabulated equations of state (EOS). An exhaustive list of publications enabled by FUKA is routinely updated here [55]. FUKA also provides a robust, minimal interface for exporting ID solutions to evolution codes, allowing easy access to the interpolated solution. To date, FUKA has been coupled to the latest state of the art codes including, the Einstein Toolkit [56], SpECTRE [57], BAM [58], SACRA [59], SPHINCS\_BSSN [60], MHDuet [61], and GROovy [62] as well as others [63].

In this work we take a first step towards providing high-accuracy ID for differentially rotating neutron stars by extending the FUKA suite of ID solvers [54] to compute isolated neutron star (NS) ID with differential rotation, while maintaining the high accuracy and efficiency of spectral methods. To do so, we leverage Quasi-Isotropic Coordinates (QIC) and the eXtended Conformal Thin Sandwich (XCTS) formulations to solve the Einstein constraint equations. These approaches help to minimize the computational resources required for ID generation and allow for multiple means of self-validation. To this end, we have extended FUKA to compute isolated NS solutions using QIC, and extended both QIC and XCTS NS solvers to support differential rotation via the KEH law. Here QIC is particularly useful as it reduces the system of equations to essentially a 2D problem, but is restricted to axisymmetric solutions, whereas XCTS is a generic formulation that can be applied to non-axisymmetric configurations.

In this work, we aim to: (i) compute and validate high-order, spectrally accurate KEH solutions using the QIC and XCTS formulations within FUKA; (ii) establish code-verification pathways against published results and independent tools that have historically adopted KEH-based sequences; and (iii) validate the accuracy and effectiveness of each implementation using dynamical simulations. To do so, we build upon KADATH’s multi-domain spectral scheme with compactified outer boundaries, and on FUKA’s robust solving framework. Furthermore, we extend FUKA’s existing EOS support to include the use of 3D tabulated EOS using GRHayLEOS [64], the first known implementation in a public code.

The remainder of this paper is organized as follows: Section II reviews the mathematical framework (3+1 decomposition, QIC and XCTS formulations, hydro-stationary equilibrium and the KEH rotation law). Section III describes the numerical implementation of the initial data solvers. Section IV outlines the methods used to conduct dynamical simulations using the computed ID solutions. Section V reports verification and validation results, including cross-formulation analysis and comparison with published results. Finally, section VI summarizes our findings and outlines possible avenues for future research and extensions to FUKA.

## II. MATHEMATICAL BACKGROUND

To simulate astrophysical events using general relativity a key mechanism is to decompose Einstein’s field equations using the standard 3 + 1 decomposition whereby the spacetime line element takes the form [65, 66]

$$ds^2 = -\alpha^2 dt^2 + \gamma_{ij}(dx^i + \beta^i dt)(dx^j + \beta^j dt), \quad (1)$$

$$n_\mu \equiv -\alpha \nabla_\mu t, \quad (2)$$

$$\gamma_{\mu\nu} = g_{\mu\nu} + n_\mu n_\nu, \quad (3)$$

where  $\alpha$  is known as the *lapse*,  $\beta^i$  is the *shift*,  $n_\mu$  is the unit normal to the three dimensional hypersurface  $\Sigma_t$ , and  $\gamma_{ij}$  is the purely spatial metric compatible with  $\Sigma_t$ . Using this decomposition, Einstein’s field equations can then be recast into the form

$$R + K^2 - K_{ij}K^{ij} = 16\pi E, \quad (4)$$

$$D_j K^j_i - D_i K = 8\pi P_i, \quad (5)$$

which is an elliptic system of equations regarded as the initial value problem in numerical relativity. Here  $R$  is the Ricci scalar,  $K_{ij}$  is the extrinsic curvature of  $\Sigma_t$ , and  $K$  is the trace of  $K_{ij}$ , commonly referred to as the mean curvature. The right hand side (RHS) includes source terms of the total energy  $E$  and the momentum current  $P_i$ , which are defined using projections of the energy-momentum tensor  $T^{\mu\nu}$ .

We approximate stellar material as a perfect fluid, where  $T^{\mu\nu}$  takes the form

$$T^{\mu\nu} \equiv \rho u^\mu u^\nu + p g^{\mu\nu}, \quad (6)$$

with  $\rho$  being the rest-mass density,  $h \equiv 1 + \epsilon + p/\rho$  the relativistic specific enthalpy,  $u^\mu$  the fluid four-velocity, and  $p$  the pressure. By decomposing  $T^{\mu\nu}$  using the 3+1 decomposition, we obtain the following contractions along time-like and space-like directions

$$E \equiv T_{\mu\nu} n^\mu n^\nu, \quad (7a)$$

$$P_\alpha \equiv -T_{\mu\nu} \gamma^\mu{}_\alpha n^\nu, \quad (7b)$$

$$S_{\alpha\beta} \equiv T_{\mu\nu} \gamma^\mu{}_\alpha \gamma^\nu{}_\beta. \quad (7c)$$

With these projections and a choice of coordinates, we can endeavour to compute the initial data solution for an astrophysical system of interest at a given instant in time.

To compute a stationary, axisymmetric spacetime, it is necessary to define a Killing vector field  $\xi^\mu$  that exhibits these symmetries. This is equivalent to finding a vector field that is a solution to Killing's equation

$$\nabla_\xi g_{\mu\nu} = 0. \quad (8)$$

Under a 3+1 decomposition, we can express the Killing vector as

$$\xi^\mu = \alpha n^\mu + \beta^\mu. \quad (9)$$

For a stationary and axisymmetric spacetime, the Killing vector field can be expressed as [67]

$$\xi^\mu = \alpha n^\mu + \Omega \chi^\mu, \quad (10)$$

where  $\chi^\mu$  is the rotational Killing vector field. In the case of a perfect fluid that is not rotating or is experiencing circular flows, the four-velocity of a zero angular momentum observer (ZAMO) is given by

$$u^\mu = W [n^\mu + U^\mu], \quad (11)$$

$$U^\mu \equiv \frac{1}{\alpha} (\Omega \chi^\mu + \beta^\mu), \quad (12)$$

$$W \equiv \frac{1}{\sqrt{1 - \gamma_{\mu\nu} U^\mu U^\nu}}, \quad (13)$$

where  $W$  is the Lorentz factor with respect to a ZAMO,  $U^\mu$  the fluid 3-velocity measured by a ZAMO,  $\Omega$  is the angular velocity profile of the fluid, and  $\chi^\mu = \partial_\varphi$  is the rotation Killing vector field for an axisymmetric spacetime.

### A. Quasi-isotropic coordinates

A common choice of coordinates in numerical relativity are quasi-isotropic coordinates (QIC)  $(t, r, \theta, \varphi)$ , which preserve the axisymmetric nature of the system while allowing for non-spherically symmetric solutions [67, 68]. For QIC,  $\gamma_{ij} = (A^2, A^2, B^2 r^2 \sin^2 \theta)$  and  $\beta^i = (0, 0, -\omega)$ , yielding the following spacetime metric

$$g_{\mu\nu} dx^\mu dx^\nu = -\alpha^2 dt^2 + A^2 (dr^2 + r^2 d\theta^2) + B^2 r^2 \sin^2 \theta (d\varphi + \beta^\varphi dt)^2. \quad (14)$$

With this coordinate choice and the use of  $\omega = -\beta^\varphi$ , (4) and (5) can be rewritten in a form that is more suitable for numerical solutions [67, 69];

$$\Delta_3 \nu = \frac{B^2 r^2 \sin^2 \theta}{2\alpha^2} \partial\omega \partial\omega - \partial\nu \partial(\nu + \ln B) + 4\pi A^2 (E + S), \quad (15a)$$

$$\tilde{\Delta}_3 (\omega r \sin \theta) = -16\pi \frac{\alpha A^2}{B^2} \frac{P_\varphi}{r \sin \theta} + r \sin \theta \partial\omega \partial(\nu - 3 \ln B), \quad (15b)$$

$$\Delta_2 (\ln A + \nu) = \frac{3B^2 r^2 \sin^2 \theta}{4\alpha^2} \partial\omega \partial\omega - \partial\nu \partial\nu + 8\pi A^2 S_\varphi^\varphi, \quad (15c)$$

$$\Delta_2 [(\alpha B - 1) r \sin \theta] = 8\pi \alpha A^2 B r \sin \theta (S_r^r + S_\theta^\theta), \quad (15d)$$

$$\Delta_3 \equiv \frac{\partial^2}{\partial r^2} + \frac{2}{r} \frac{\partial}{\partial r} + \frac{1}{r^2} \frac{\partial^2}{\partial \theta^2} + \frac{1}{r^2 \tan \theta} \frac{\partial}{\partial \theta}$$

$$\tilde{\Delta}_3 \equiv \Delta_3 - \frac{1}{r^2 \sin^2 \theta},$$

$$\Delta_2 \equiv \frac{\partial^2}{\partial r^2} + \frac{1}{r} \frac{\partial}{\partial r} + \frac{1}{r^2} \frac{\partial^2}{\partial \theta^2},$$

$$\partial f \partial g \equiv \frac{\partial f}{\partial r} \frac{\partial g}{\partial r} + \frac{1}{r^2} \frac{\partial f}{\partial \theta} \frac{\partial g}{\partial \theta},$$

where  $\nu \equiv \ln \alpha$ ,  $\Delta_3$  ( $\Delta_2$ ) is the 3-dimensional (2-dimensional) flat Laplacian and  $\partial f \partial g$  denotes the flat

metric scalar product of the gradients of  $f$  and  $g$ .

To model the fluid using QIC, we express the fluid 3-

velocity (12) as [67]

$$U^\mu \equiv \frac{1}{\alpha} (\Omega - \omega) \chi^\mu, \quad (16)$$

where  $\omega$  is proportional to the angular velocity of a ZAMO due to frame dragging effects of a rotating space-time. Using the definition [67]

$$U \equiv \frac{B}{\alpha} (\Omega - \omega) r \sin \theta, \quad (17)$$

and the fact that  $\chi \cdot \chi = B^2 r^2 \sin^2 \theta$ , the fluid 3-velocity has the following  $\varphi$  components [67]

$$U^\varphi = \frac{1}{\alpha} (\Omega - \omega), \quad (18)$$

$$U_\varphi = U B r \sin \theta. \quad (19)$$

$$(20)$$

With these definitions, we now express the Lorentz factor and energy-momentum tensor projections  $E$ ,  $S$ ,  $S^i{}_j$  and  $P_\varphi$  (7) as [67]

$$W^2 = \frac{1}{(1 - U^2)}, \quad (21)$$

$$E = \rho h W^2 - p, \quad (22)$$

$$P_\varphi = (E + p) U B r \sin \theta, \quad (23)$$

$$S^r{}_r = S^\theta_\theta = p, \quad (24)$$

$$S^\varphi_\varphi = p + (E + p) U^2, \quad (25)$$

$$S = 3p + (E + p) U^2. \quad (26)$$

## B. eXtended Conformal Thin Sandwich (XCTS)

In the case of compact objects with source terms, especially those that include magnetic fields or in compact configurations such as binary systems, the underlying degrees of freedom of the system are not readily apparent. An incredibly successful ansatz is that of a conformal decomposition of the spatial metric [70–72] such that

$$\gamma_{ij} \equiv \Psi^4 \tilde{\gamma}_{ij}, \quad (27)$$

where  $\tilde{\gamma}_{ij}$  is a background metric and  $\Psi$  is the conformal factor that describes how the local region deviates from the background metric. The extrinsic curvature can also be decomposed into a trace free form [72]

$$K_{ij} = A_{ij} + \frac{1}{3} K \gamma_{ij}, \quad (28)$$

$$A_{ij} = \Psi^{-10} \hat{A}_{ij}, \quad (29)$$

$$\hat{A}^{ij} \equiv \frac{\Psi^6}{2\alpha} (\tilde{D}^i \beta^j + \tilde{D}^j \beta^i - \frac{2}{3} \tilde{\gamma}^{ij} \tilde{D}_k \beta^k - \partial_t \tilde{\gamma}^{ij}), \quad (30)$$

where the exponent of  $\Psi$  is chosen to be consistent with the computed result from the momentum constraint (cf. [65], Sec. 6.5.2 for a discussion). By utilizing (27), (29),

and (30) we can rewrite (4) & (5) into what is known as the Conformal Thin Sandwich decomposition (CTS):

$$\begin{aligned} \tilde{D}^k \tilde{D}_k \Psi + \frac{1}{8} \Psi^{-7} \hat{A}_{ij} \hat{A}^{ij} + 2\pi \Psi^5 E \\ - \frac{1}{8} \tilde{R} \Psi - \frac{1}{12} K^2 \Psi^5 = 0, \end{aligned} \quad (31)$$

$$\begin{aligned} \tilde{D}_j \left( \frac{\Psi^6}{\alpha} (\tilde{\mathbb{L}}\beta)^{ij} \right) + D_j \left( \frac{\Psi^6}{\alpha} \partial_t \gamma^{ij} \right) \\ - \frac{4}{3} \Psi^6 \tilde{D}^i K - 16\pi \alpha \Psi^4 P^i = 0, \\ (\tilde{\mathbb{L}}\beta)^{ij} \equiv \tilde{D}^i \beta^j - \tilde{D}^j \beta^i - \frac{2}{3} \tilde{\gamma}^{ij} \tilde{D}_k \beta^k. \end{aligned} \quad (32)$$

The remaining degrees of freedom yet to be specified are the conformal metric  $\tilde{\gamma}_{ij}$  and its time derivative; the mean curvature  $K$  and its time derivative; the lapse function  $\alpha$ ; and the source terms  $E$  and  $P^i$ . In this work we restrict ourselves to the conformally flat approximation such that conformal spatial metric in Cartesian coordinates is  $\tilde{\gamma}_{ij} = \delta_{ij}$  and  $\partial_t \tilde{\gamma}_{ij} = 0$ . Furthermore, we assume maximal slicing for adjacent hypersurfaces such that  $K = \partial_t K = 0$ . An extension to the CTS system was made in [73] where an elliptic constraint equation is obtained for the lapse yielding

$$\begin{aligned} \tilde{D}_i \tilde{D}^i (\alpha \Psi) + \Psi^5 (\partial_t K - \beta^i \tilde{D}_i K) \\ - \alpha \Psi \left[ \frac{1}{8} \tilde{R} + \frac{5}{12} K^2 \Psi^4 + \frac{7}{8} \Psi^{-8} \hat{A}^{ij} \hat{A}_{ij} \right. \\ \left. + 2\pi \Psi^4 (E + 2S) \right] = 0. \end{aligned} \quad (33)$$

The complete system (31), (32), and (33) is commonly referred to as the eXtended Conformal Thin Sandwich (XCTS) system of equations. Under our demand of conformal flatness and maximal slicing, (31), (32), and (33) take the form

$$\tilde{D}^k \tilde{D}_k \Psi + \frac{1}{8} \Psi^{-7} \hat{A}_{ij} \hat{A}^{ij} + 2\pi \Psi^5 E = 0, \quad (34a)$$

$$\tilde{D}_j \left( \frac{\Psi^6}{\alpha} (\tilde{\mathbb{L}}\beta)^{ij} \right) - 16\pi \alpha \Psi^4 P^i = 0, \quad (34b)$$

$$\begin{aligned} \tilde{D}_i \tilde{D}^i (\alpha \Psi) - \alpha \Psi \left[ \frac{7}{8} \Psi^{-8} \hat{A}^{ij} \hat{A}_{ij} \right. \\ \left. + 2\pi \Psi^4 (E + 2S) \right] = 0, \end{aligned} \quad (34c)$$

which are the actual equations implemented in the FUKE initial data solvers. To obtain the source terms  $E$ ,  $S$ , and  $P^i$ , we first find the fluid 3-velocity  $U^i$  and Lorentz factor  $W$  in Cartesian coordinates using (12) and (13)

$$U^i = \frac{1}{\alpha} (\beta^i + \Omega \xi^i), \quad (35)$$

$$W = (1 - \Psi^4 U^i U_i)^{-1/2}. \quad (36)$$

With these definitions, we can compute the source terms (7)

$$E = \rho h W^2 - p, \quad (37a)$$

$$S^i_i = 3p + (E + p)U^2, \quad (37b)$$

$$P^i = \rho h W^2 U^i. \quad (37c)$$

### C. Hydrostatic equilibrium

To solve for a neutron star in hydrostatic equilibrium, we enforce the conservation equations (see [54] for a detailed discussion)

$$\nabla_\mu T^{\mu\nu} = 0, \quad (38)$$

$$\nabla_\mu (\rho u^\mu) = 0. \quad (39)$$

By expanding (38) for an isentropic fluid, we obtain

$$u^\mu \nabla_\mu (h u_\nu) + \nabla_\nu h = 0. \quad (40)$$

For a stationary spacetime where the fluid is undergoing stationary, circular motion, the first integral of motion reduces to [20, 67]

$$\nabla_\mu \left[ \ln \left( \frac{\alpha h}{W} \right) \right] + j \nabla_\mu \Omega = 0, \quad (41)$$

$$(42)$$

where  $j \equiv u^t u_\varphi$  and is defined for QIC and XCTS coordinates as

$$j_{\text{QIC}} = \frac{W^2}{\alpha} U_\varphi, \quad (43)$$

$$j_{\text{CART}} = \frac{W^2}{\alpha} \Psi^4 U_i \chi^i, \quad (44)$$

In the case of rigid rotation, (41) reduces to

$$\ln \alpha + \ln h - \ln W = C, \quad (45)$$

where  $C$  is a constant of integration. However, in the case of differential rotation, (41) must be solved by determining the integral of the fluid rotation profile,  $j \nabla_\mu \Omega$  [20, 67]. Within FUKA, we have included the differential rotation model of *Komatsu, Eriguchi, and Hachisu* (KEH), also known as the  $j$ -constant model

$$\Omega = \Omega_c - \frac{j}{\mathcal{A}^2}, \quad (46)$$

where  $\mathcal{A}$  is a parameter that controls the degree of differential rotation and  $\Omega_c$  is the rotation velocity at the stellar center. In the limit of  $\mathcal{A} \rightarrow \infty$ , the KEH model reduces to a rigidly rotating star. In order to find a solution for  $\mathcal{A}$  and  $\Omega_c$ , we must also specify the ratio of the polar to equatorial radius of the star ( $r_p/r_e$ ) along with the ratio  $\hat{\mathcal{A}} \equiv \mathcal{A}/r_e$ . For this model, an analytical first integral is available for the rotation profile resulting in a first integral of motion of the form

$$\ln \alpha + \ln h - \ln W - \frac{1}{2} \frac{j^2}{\mathcal{A}^2} = C. \quad (47)$$

To close the system of equations, an equation of state (EOS) must also be specified. Within FUKA one can utilize (piecewise-)polytropic EOSs, cold tabulated EOSs in the standard LORENE format, or 3D tabulated EOSs in *stellar collapse* format [74]. Support for 3D tabulated EOS is provided by the GRHayL library [64, 75], which has been recently incorporated into FUKA. We note that the current use of GRHayLEOS is restricted to the cold beta-equilibrium slice of the 3D EOS table. The reason for this is twofold: (i) the EOS module in FUKA assumes an isentropic fluid ( $ds = 0$ ) and (ii) GRHayLEOS only supports computing constant temperature, beta-equilibrium slices of the EOS table. Future work will include support for constant entropy slices of the EOS table as well as removing the assumption of an isentropic fluid in FUKA to enable the self-consistent study of hot stars.

### D. Diagnostics

To reliably fix the characteristics of the NS, we need to compute specific diagnostic quantities. To fix the mass of the NS, we either fix fluid quantities at the center of the star (e.g., central rest-mass density or central specific enthalpy) or the total gravitational mass of the NS. The latter is fixed by computing the ADM mass of the system. In FUKA, this is performed by computing a surface integral on the outer boundary of the outermost domain. This domain leverages a compactified coordinate system such that  $r = \infty$  is mapped to a finite value [53]. In this way, we can reliably compute the ADM mass in the weak field limit using

$$M_{\text{ADM}}^{\text{QIC}} = -\frac{1}{4\pi} \int_{S_\infty} \partial_i B ds^i, \quad (48)$$

$$M_{\text{ADM}}^{\text{XCTS}} = -\frac{1}{2\pi} \int_{S_\infty} D_i \Psi ds^i. \quad (49)$$

As a consequence of fixing the mass of the star using the ADM mass or central fluid quantities, it is possible to compute the total rest-mass of the star by computing the following volume integral over the stellar domains:

$$M_{\text{b}} = \int_V W \rho \sqrt{\gamma} dx^3. \quad (50)$$

Additional diagnostics beneficial for analyzing the 1D solutions and comparing to previous literature include the total internal energy  $E_{\text{int}}$ , the total angular momentum  $J$ , the rotational kinetic energy  $T$ , the gravitational binding energy  $\mathcal{W}$  and the instability parameter,

$\beta^2$  [76, 77]

$$E_{\text{int}} = \int_V W \rho \epsilon \sqrt{\gamma} dx^3, \quad (51)$$

$$J = \int_V \rho j \alpha \sqrt{\gamma} dx^3, \quad (52)$$

$$T = \frac{1}{2} \int_V \Omega \rho j \alpha \sqrt{\gamma} dx^3, \quad (53)$$

$$\mathcal{W} = T + E_{\text{int}} + M_b - M_{\text{ADM}}, \quad (54)$$

$$\beta = \frac{T}{|\mathcal{W}|}. \quad (55)$$

### E. Boundary Conditions

To close the system of equations, appropriate boundary conditions must be imposed. At the outer boundary of the computational domain, we impose the weak-field conditions on metric variables, such that for XCTS:

$$\lim_{r \rightarrow \infty} \alpha = 1, \quad (56)$$

$$\lim_{r \rightarrow \infty} \Psi = 1, \quad (57)$$

$$\lim_{r \rightarrow \infty} \beta^i = 0, \quad (58)$$

and for QIC:

$$\lim_{r \rightarrow \infty} \nu = 0, \quad (59)$$

$$\lim_{r \rightarrow \infty} (\ln A + \nu) = 0, \quad (60)$$

$$\lim_{r \rightarrow \infty} (\alpha B - 1)r \sin \theta = 0, \quad (61)$$

$$\lim_{r \rightarrow \infty} (\omega r \sin \theta) = 0. \quad (62)$$

To ensure the surface of the star corresponds to a domain boundary, we set the boundary condition for the adapted domain shells to be defined by

$$\ln h = 0. \quad (63)$$

## III. IMPLEMENTATION DETAILS

The FUKA suite of initial data codes is built on an extended version of the KADATH spectral library [53], a robust framework designed for solving elliptic systems of equations using spectral methods. The relevant features of KADATH critical to this work include its novel interface for implementing equations and constraints in a L<sup>A</sup>T<sub>E</sub>X-like syntax, which are then automatically converted into numerical algorithms that are solved using spectral methods.

<sup>2</sup> We use  $\beta$  to denote the instability parameter to be consistent with previous literature, however; it should not be confused with the shift vector,  $\beta^i$ .

KADATH utilizes a novel domain decomposition that adopts a nucleus domain with a well-defined coordinate system across and including  $r = 0$ , adapted domain shells that allow for non-spherical/circular objects (i.e., rotating neutron stars) and exterior domain shells that use compactified coordinates such that  $r = \infty$  (i.e., the weak-field limit) maps to a finite value. Use of adapted shells is essential for numerical stability, so that the stellar surface can be defined at the grid interface. This results in reduced spectral noise, known as Gibbs phenomenon, which occurs when attempting to model discontinuities using a single spectral expansion.

Systems of equations within KADATH are solved using a Newton-Raphson method, employing automatic differentiation to efficiently compute derivatives of fields in parallel. The Newton-Raphson method is used in conjunction with a tau method, to find spectral coefficients that minimize the residual of the constraint equations. In FUKA, a stopping criterion of  $\varepsilon_{\text{STOP}} \equiv 10^{-8}$  is used.

### A. QIC Solver

To compute solutions of the QIC system of equations<sup>3</sup>, FUKA utilizes KADATH's support for polar coordinate systems, which are incredibly efficient for solving problems with circular axial symmetry (see Ref. [68] for details). This reduces the dimensionality of the problem to 2D, and significantly reduces the degrees of freedom.

The physical space is decomposed into numerical domains including a polar nucleus domain that covers the center of the star followed by two adapted polar shells that adapt to the stellar surface. An outer compactified polar shell is used to impose the boundary conditions in the weak-field limit. All domains are matched at domain interfaces where the boundary conditions simply enforce continuity of the fields and their normal derivatives.

To initialize the fluid and spacetime fields, FUKA utilizes a 1D Tolman–Oppenheimer–Volkoff (TOV) solution of an isolated, non-rotating star using the same EOS and target mass. If the desired mass is not supported by the TOV solver, the maximum mass for the EOS ( $M_{\text{TOV}}$ ) is used and the desired mass is attempted to be found once the desired rotation profile is found. FUKA then solves the QIC system of equations (15) in conjunction with thermodynamic constraint equations (45) for a non-rotating star. Once a solution is found, a uniform rotation profile (e.g.,  $\chi = 0.1$ ) is solved for. This is important, as the differential rotation parameters only specify the shape of the star and the degree of differential rotation, but not the direction. Therefore, the Newton-Raphson solver will quickly diverge if attempting to solve for a differentially rotating star directly. Finally, once a uniformly rotating solution is found, the axis ratio ( $r_p/r_e$ ) is incrementally decreased to the desired value for a fixed value of  $\hat{\mathcal{A}}$ .

<sup>3</sup> In the FUKA repo, the solver is called *NS\_isotropic*

The simplicity of the QIC system combined with the efficiency of KADATH’s spectral solver enables the QIC solver to run on moderate system resources (e.g., quad-core CPU and  $\sim 16$  GB of computer memory). Even at high resolutions, solutions can be computed in minutes, and sequences of equilibrium solutions, such as those presented in Fig. 3, take less than an hour to compute.

## B. XCTS Solver

In the case of solving the 3D XCTS system of equations, FUKA utilizes Cartesian coordinates for physical quantities within KADATH’s spherical domain decomposition, whereas a spectral expansion over  $(r, \theta, \varphi)$  for the radial, polar, and azimuthal directions are used for the numerical coordinates.

The physical space is decomposed in a similar fashion to the QIC space, only now 3D spherical domains are used instead, i.e., a spherical nucleus domain, two adapted spherical shells, and an outer compactified spherical shell. The boundary conditions are imposed in a similar manner as the QIC solver for the relevant fields.

While the XCTS system is a flexible system of equations and open to extension to a variety of physical systems (e.g., binary initial data, misaligned spins, magnetic fields, etc.,) [54, 78, 79], it is computationally expensive. Beyond coarse resolution models, high resolution solutions even for isolated neutron stars can take hours/days to compute on a personal computer with sufficient memory.

As we will demonstrate in Sec. V, the QIC and XCTS solutions are in excellent agreement and approximately recover the same physical metric and fluid quantities. Therefore, we utilize a hybrid approach to compute NS solutions using the XCTS system of equations in the publicly available codes<sup>4</sup>. To do so, we first compute the desired solution using the QIC solver. Using FUKA’s export interface for QIC solutions, we obtain the physical metric and fluid quantities in Cartesian coordinates. Next, we initialize the XCTS fields by interpolating the QIC solution at the Cartesian coordinates of the XCTS collocation points. Here we approximate the conformal factor as  $\Psi^4 = \gamma_{xx}$ . Once the fields are initialized, FUKA will solve the XCTS system of equations Eq. ((34a) – (34c)) and thermodynamic constraints for the desired solution directly (non-rotating, uniformly rotating, or differentially rotating) based on the QIC solution, thus significantly reducing the computational time to find an XCTS solution.

## C. Resolution

The spectral resolution in FUKA is currently specified by the user using a single quantity,  $res(R)$ . For QIC solutions,  $res$  specifies the number of collocation points in  $r$  and  $\theta$  directions per domain,  $(R, R)$ . For XCTS solutions,  $res$  specifies the number of collocation points in  $r$ ,  $\theta$ , and  $\varphi$  directions per domain,  $(R, R, R-1)$ . While angular resolution plays an important role in resolving the deformed star, the radial resolution is essential for comparing ID solutions and understanding when spectral noise begins to deteriorate the solution.

An additional quantity that will prove useful in Sec. V is the effective spectral resolution,  $\tilde{N}$ , which we define as

$$\tilde{N} \equiv (D/3)N^{1/D}, \quad (64)$$

$$N \equiv \sum_{i=1}^d \prod_{j \in r, \theta, \varphi} N_j^{(i)}, \quad (65)$$

where  $N_j^{(i)}$  is the number of collocation points in the  $j$ -th direction of the  $i$ -th domain,  $d$  is the number of domains, and  $D$  is the number of spatial dimensions (i.e.,  $D = 2$  for QIC and  $D = 3$  for XCTS). The effective spectral resolution provides an estimate of the average number of collocation points per direction across all domains and provides an additional means to effectively compare QIC and XCTS solutions in Sec. V.

## IV. METHODS — DYNAMIC SIMULATIONS

To validate initial data solutions computed using FUKA, we must examine the impact of the ID solution on the dynamical behavior of the NSs after evolution. To this end we utilize the public evolution framework, the `Einstein Toolkit` [56], and the fixed-mesh box-in-box refinement driver [81]. Within the `Einstein Toolkit`, we make use of the general relativistic magnetohydrodynamics (GRMHD) code `IllinoisGRMHD` [82] to evolve the hydrodynamic quantities coupled to the spacetime evolution provided by the `Baikal` thorn.

Baikal employs the BSSN formulation [83–85], where we specify the use of fourth order finite differencing, and employ the fourth-order Runge-Kutta timestepping algorithm to evolve the coupled matter-spacetime system, as implemented in the `Einstein Toolkit`, using a Courant factor of 0.2. For the spacetime evolution we also employ fifth order Kreiss-Oliger dissipation [86], with strength 0.2, and use the moving puncture gauge condition, with gamma-driving shift [87–89]. For outer boundary conditions we use outgoing radiation boundary conditions using the `NewRad` thorn, while `IllinoisGRMHD` enforces outflow boundary conditions on the fluid velocity.

Here we validate the ID solutions computed in FUKA by computing and evolving polytropic models SB6 and U13, which have been thoroughly studied in the literature [80] (see Tab. I). For these models we use `IllinoisGRMHD`

<sup>4</sup> In the FUKA repo, the solver is called `NS_DIFFROT`

TABLE I. Comparison of the **SB6** and **U13** models between XCTS and QIC solvers at resolutions  $R \in \{11, 13, 17\}$  against reference values from Ref. [80]. Here we list the instability parameter  $\beta$ , central density  $\rho_c$ , and dimensionless angular momentum  $J/M^2$  for each model. **SB6** is fixed using  $r_p/r_e = 0.336$ ,  $\hat{A} = 1$ , and  $M_{ADM} = 1.449$ . **U13** is fixed using  $r_p/r_e = 0.20012$ ,  $\hat{A} = 1$ , and  $M_{ADM} = 1.462$ . **SB6** and **U13** utilize a polytropic EOS with  $\Gamma = 2$  and  $K = 100$  whereas **SLy.SB6** and **SLy.U13** utilize the **SLy** 3D tabulated EOS.

SB6	$\beta$	$\rho_c [10^4]$	$J/M^2$	U13	$\beta$	$\rho_c [10^5]$	$J/M^2$
Ref. [80]	0.240	2.261	1.411	Ref. [80]	0.281	5.990	1.753
XCTS.R11	0.236	2.261	1.410	XCTS.R11	0.285	5.983	1.738
XCTS.R13	0.236	2.261	1.411	XCTS.R13	0.278	5.995	1.791
XCTS.R17	0.236	2.261	1.410	XCTS.R17	0.279	5.992	1.760
QIC.R11	0.234	2.263	1.410	QIC.R11	0.276	5.959	1.746
QIC.R13	0.234	2.263	1.413	QIC.R13	0.274	6.008	1.754
QIC.R17	0.234	2.263	1.413	QIC.R17	0.274	5.996	1.754
<b>SLy.SB6</b>				<b>SLy.U13</b>		$\rho_c [10^4]$	
XCTS.R11	0.226	6.819	1.136	XCTS.R11	0.276	3.510	1.449
XCTS.R13	0.228	6.797	1.133	XCTS.R13	0.266	3.484	1.315
XCTS.R17	0.229	6.801	1.134	XCTS.R17	0.272	3.490	1.349

presented in Ref. [82] with the same equation of state parameters as the initial data models. We note that **IllinoisGRMHD** uses a hybrid equation of state of the form

$$P = K\rho^\Gamma + (\Gamma_{th} - 1)\rho\epsilon_{th}, \quad (66)$$

where  $\epsilon_{th}$  is the thermal contribution to the internal energy originating from shocks. Therefore we set  $\Gamma_{th} = \Gamma$  in the tests presented here.

For each simulation we use a constant density atmosphere  $\rho_{atm} = 1.28 \times 10^{-12}$  and exclude magnetic field evolution, similar to the studies presented in [77, 90].

Each configuration is evolved for  $\sim 30$ ms using two resolutions in order to confirm convergence of the ID models in an evolution scheme. For our medium resolution ( $\Delta_{Mx}$ ), we use only two refinement levels centered on the neutron star, with the coarse grid having a resolution  $dx = 0.8$  with side-lengths 204.8 in all three directions. In our evolution of these models we do not impose any symmetries, and only allow truncation errors to drive the bar-mode instability. For our high resolution simulations ( $\Delta_{Hx}$ ) we decrease the grid spacing on both refinement levels by 20%, where the coarse grid has resolution  $dx = 0.64$ .

We have chosen to use **SB6** (**U13**) models as they are stable (unstable) against the dynamical bar mode instability, where the NS becomes deformed into a bar-like configuration. During this transient period, the NS expels matter and redistributes angular momentum, until relaxing into a new stable configuration. The study presented in [77] demonstrated that models of rapidly rotating NS with a rotation profile described by the KEH law will be susceptible to the instability if the  $\beta = T/|W|$  parameter exceeds some critical value. To track the growth and saturation of the instability during dynamical evolution, we monitor the azimuthal Fourier modes using

$$P_m = \int_V d^3x \rho e^{im\varphi}. \quad (67)$$

The bar-mode instability is characterized by an exponential increase in the  $m = 2$  mode [80]. To this end, we measure  $P_m$  out to a radius of  $r = 45$  throughout the time evolution.

Finally, we aim to validate solutions computed with **FUKA** using a finite-temperature, tabulated equation of state, using the same methods for dynamical evolution only now with the **SLy** EOS [91]. Since existing literature has not focused on the bar-mode instability with realistic EOS, we construct similar models to the polytropic cases presented above, such that a stable and unstable model are obtained (see Tab. I), however, we focus solely on the unstable model computed with the XCTS solver as this proved sufficient to validate the solutions computed with **FUKA**. For these tests we utilize the tabulated EOS version of **IllinoisGRMHD** as described in [92], with the electron fraction within the star initialized based on the beta-equilibrium cold slice.

## V. RESULTS

Here we present the initial data and time evolution results using QIC and XCTS solutions. We will begin with a self-consistency test of the XCTS and QIC solvers independently followed by a comparison of the agreement between the two solvers. With confidence in the equivalence of the two solvers, we will compare the QIC solution against the **Hydro-RNS** thorn from the **Einstein Toolkit**, derived from the **RNS** code [28, 93] for a variety of differential rotation profiles. Additionally, we will present a rigorous analysis of the time evolution of the

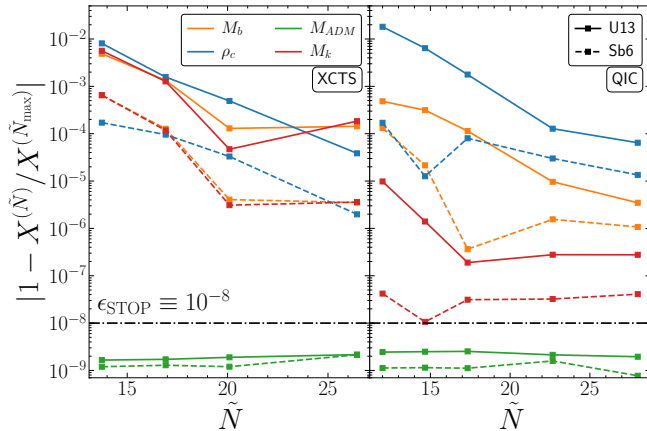


FIG. 1. Self-convergence of the XCTS (*left*) and QIC (*right*) solvers for U13 and SB6 configurations, respectively. Exponential convergence is observed up to  $\tilde{N} \sim 22$  at which point the error is dominated by spectral noise and solutions begin to deteriorate. We include  $\epsilon_{\text{STOP}} \equiv 10^{-8}$ , the stopping threshold for the Newton-Raphson solver in KADATH, to highlight the expected precision floor.

QIC and XCTS solutions for configurations that are bar-mode (un)stable and compare to previously published results. Finally, we will present novel results using dynamical simulations of a bar-mode unstable configuration using a realistic, tabulated EOS.

For the results presented using a polytropic EOS (see Tab. I), we utilize the SB6 and U13 configurations which have been thoroughly studied previously [80]. In this case, the EOS is a simple polytrope with a polytropic index of  $\Gamma = 2$  and a polytropic constant of  $K = 100$ .

### A. Initial Data Convergence

A key feature of using spectral methods is the ability to achieve exponential convergence of the solution as the number of collocation points is increased. To verify this, we compute a series of solutions for both the SB6 and U13 configurations at increasing resolutions using the XCTS and QIC solvers. For a given effective resolution  $\tilde{N}$  as defined using (64), we compute the ADM mass ( $M_{\text{ADM}}$ ), the Komar mass ( $M_k$ ), the baryonic mass ( $M_b$ ), and the central rest-mass density ( $\rho_c$ ). Finally, we compute the relative difference of each quantity with respect to the highest resolution solution for each configuration and solver. In Fig. 1, we illustrate the self-convergence of the SB6 (dashed line) and U13 (solid) configurations, using the XCTS (left) and QIC (right) solvers. Included in the plot is a horizontal line denoting the stopping threshold of the Newton-Raphson solver in FUKA,  $\epsilon_{\text{STOP}} \equiv 10^{-8}$ .

Both XCTS and QIC solutions exhibit the expected exponential convergence up to  $\tilde{N} \sim 22$  at which point the error is dominated by spectral noise and the solution begins to deteriorate. We find that the QIC solver exhibits

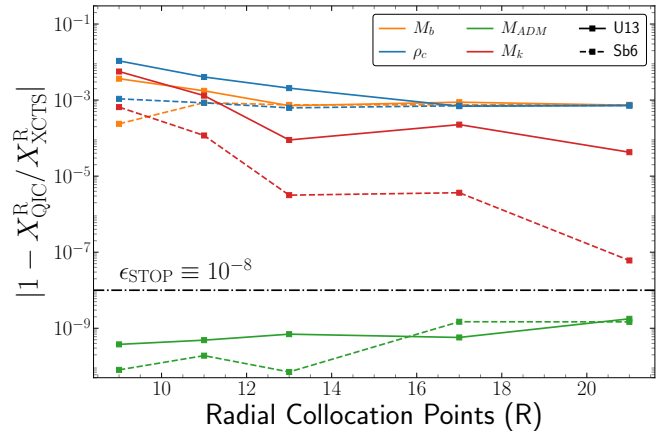


FIG. 2. Comparison between diagnostic quantities computed using QIC and XCTS solutions for a range of radial collocation points  $R$ . We find excellent agreement of  $M_k$  and  $M_{\text{ADM}}$  as the radial resolution is increased, however, fluid quantities such as  $M_b$  and  $\rho_c$  only show convergence up to  $10^{-3}$ .

considerably better convergence properties compared to the XCTS solver. This is primarily attributed to the reduced spectral noise given the spectral bases for QIC is only a product of two coordinate bases rather than three for XCTS. Additionally, the reduced dimensionality and computational complexity of the QIC system also contributes to the improved convergence properties. Finally, we note that the ADM mass, which is used as a fixing parameter for each configuration, lies well below  $\epsilon_{\text{STOP}}$ , indicating that the solvers are able to find a solution that is consistent with the desired mass of the configuration.

To compare the solutions obtained from the QIC solver against those from the XCTS solver, we use instead the radial collocation point resolution  $R$  instead of the effective resolution  $\tilde{N}$  to make a more direct comparison. Using the solutions computed previously, we calculate the relative difference of the QIC and XCTS solutions for the same diagnostic quantities as a function of  $R$ , which is illustrated in Fig. 2. While we find excellent agreement of the ADM and Komar masses, the fluid quantities,  $M_b$  and  $\rho_c$ , only agree to  $\sim 10^{-3}$ . This points to either an inaccurate comparison due to differences in effective resolution or systematic differences due to the underlying numerical methods and system of equations. Overall, we conclude that the solutions computed by the XCTS and QIC solvers are consistent and achieve the desired accuracy.

Finally, we list in Tab. I the key diagnostic quantities for the SB6 and U13 configurations computed using both the XCTS and QIC solvers for the resolutions considered, alongside the reference values from Ref. [80]. Overall we find excellent agreement between both solvers and the reference values on the order of three significant figures.

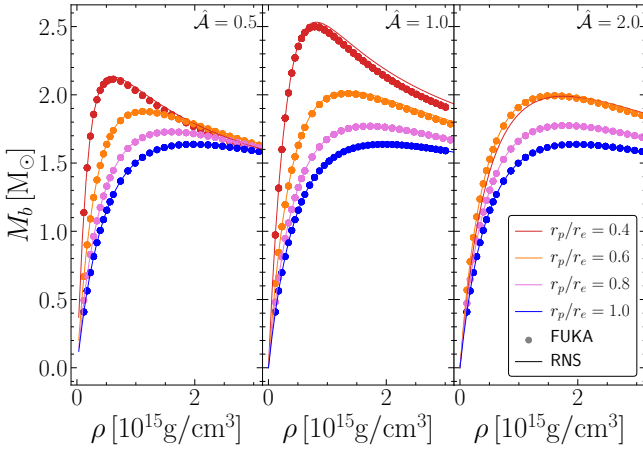


FIG. 3. Comparison of solutions between the FUKA QIC solver (circles) and the RNS code (solid lines). Here we explore a range of differential rotation profiles  $\hat{A} = \{0.5, 1.0, 2.0\}$  (left, middle, right panes, respectively) and axis ratios  $r_p/r_e = \{0.4, 0.6, 0.8, 1.0\}$  (red, orange, pink, and blue lines, respectively) over a range of central densities. No solutions were found with FUKA for  $\hat{A} = 2.0$  and  $r_p/r_e = 0.4$ , but the RNS solution is included for completeness and to highlight the change in behavior in this region of the parameter space.

### B. Comparison with RNS

With the confidence that the QIC solutions are self-consistent and agree with the XCTS solution, we now compare the QIC solutions against those computed using the well-established RNS code [28, 93]. In Fig. 3, we plot the baryonic mass ( $M_b$ ) as a function of the central rest-mass density ( $\rho_c$ ) for a series of solutions for  $\hat{A} = \{0.5, 1.0, 2.0\}$  (left, middle, right panes, respectively) and  $r_p/r_e = \{1.0, 0.8, 0.6, 0.4\}$  (blue, pink, orange, and red lines, respectively) over a range of central densities. Here we denote the solution computed with FUKA using circle markers, while solid lines indicate solutions computed with RNS. For all configurations, a polytropic EOS is used with  $\Gamma = 2$  and  $K = 100$ .

For  $\hat{A} = 0.5$  (left pane), we find excellent agreement between the two codes for all values of  $r_p/r_e$ . In the case of  $r_p/r_e = 0.4$ , we find that FUKA solutions become slightly less massive than those computed with RNS. For  $\hat{A} = 1.0$ , we find excellent agreement for  $r_p/r_e = 1.0$  and 0.8 with slight deviations for  $r_p/r_e = 0.6$  and stronger deviations for  $r_p/r_e = 0.4$ . Finally, for  $\hat{A} = 2.0$  we find similar agreement for  $r_p/r_e = 1.0, 0.8, \text{ and } 0.6$ , but solutions for  $r_p/r_e = 0.4$  were not able to be computed using FUKA. We note that RNS solutions for  $\hat{A} = 2.0$   $r_p/r_e = 0.4$  show interesting behavior where the stable masses are less than those for  $r_p/r_e = 0.6$ , which is in contrast to  $\hat{A} = 1.0, 0.5$ . We leave this as an open question for potential future study in order to ascertain the stability of solutions in this region of the parameter space and its utility to model astrophysically relevant systems.

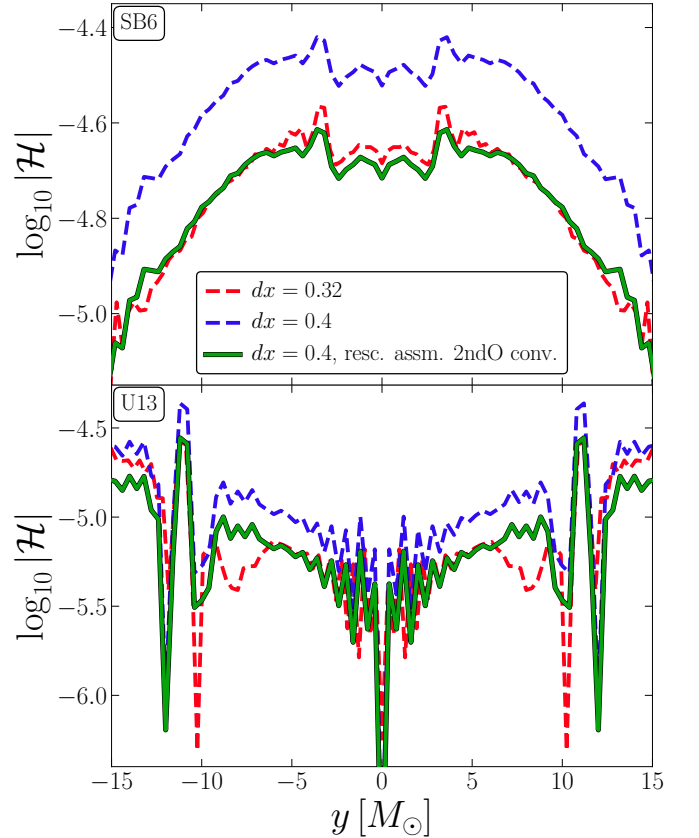


FIG. 4. Convergence analysis of the Hamiltonian constraint violations along the  $x$ -axis at  $t = 41M$  where we find the expected second-order convergence as predicted by the hydro evolution code, **IllinoisGRMHD**.

With the exception of  $\hat{A} = 2.0$   $r_p/r_e = 0.4$ , we find the solutions computed with FUKA are consistent and in agreement with those computed with RNS. The slight deviations observed for the most extreme systems exist on the unstable branch of the solution space and, thus, are likely sensitive to the numerical methods and resolution used to compute the solutions.

### C. Convergence of Dynamical Evolutions — Polytropic EOS

In this section, we present a convergence analysis of the dynamical evolution of the SB6 and U13 configurations using the **Einstein Toolkit**. To do so, we first consider initial data solutions using the FUKA XCTS solver, with resolution  $R = 17$ . The initial data is then evolved using the evolution setup described in Sec. IV, where the lowest spatial resolution used has a finest grid spacing of  $\Delta x = 0.4$ , and the highest resolution has a finest grid spacing of  $\Delta x = 0.32$ . In Fig. 4, we illustrate the Hamiltonian constraint violations along the  $x$ -axis at  $t = 41M$  for the SB6 (top) and U13 (bottom) configurations. We find the constraint violations to converge towards zero at

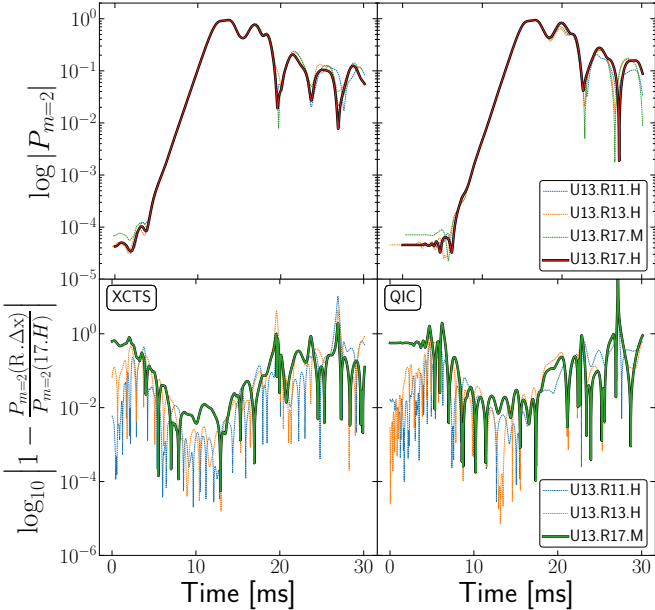


FIG. 5. *Top*: Evolution of the  $m = 2$  Fourier mode of the stellar interior for the XCTS solution (left) and QIC solution (right) for the U13 configuration. Both are consistent with behavior reported in Ref. [80]. *Bottom*: Convergence analysis of the  $m = 2$  Fourier mode of the stellar interior during dynamical evolution for the U13 configuration to assess the impact of initial data resolution  $R = \{11, 13, 17\}$  at evolution resolution  $\Delta_H x = 0.32$  and  $\Delta_M x = 0.4$ . For the QIC results, we have aligned the datasets at the onset of the bar-mode instability to focus on the long-term behavior of each configuration.

second order (green) which is expected given the algorithms used within `IllinoisGRMHD`.

In Fig. 5 we extend our analysis to further assess the impact of the initial data on the long-term dynamical evolution. Here we include a convergence analysis of the  $m = 2$  Fourier mode, a key diagnostic for assessing the growth of the bar-mode instability, for the U13 configuration (for `SB6` see Fig. 8 in Appendix A) with XCTS (left panels) and QIC (right panels) solutions, at varying initial data resolutions of  $R = \{11, 13, 17\}$ .

In the bottom panels we compute the relative difference in the power of the  $m = 2$  mode between high resolution simulations ( $\Delta_H x = 0.32$ ) using initial data resolutions  $R \in \{11, 13\}$  (referred to as U13.11.H, U13.13.H respectively) (blue, orange lines respectively) to that of the highest ID ( $R = 17$ ) and evolution resolution  $\Delta_H x = 0.32$  (referred to as U13.17.H). To determine the impact of the evolution resolution, we compute the relative difference between the highest ID resolution evolved using  $\Delta_M x = 0.4$  (referred to as U13.17.M) to that computed using  $\Delta_H x = 0.32$  (U13.17.H). For clarity, we have aligned the datasets at the onset of the bar-mode instability to focus on the long-term behavior of each configuration (see Appendix B for further discussion).

During the early evolution time of  $t \lesssim 5\text{ms}$ , we find

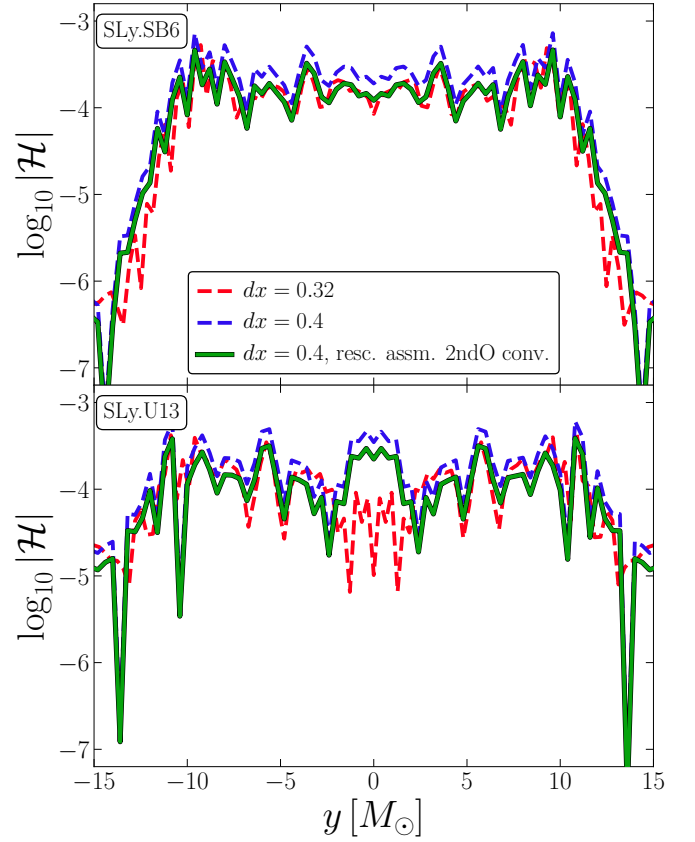


FIG. 6. Same as Fig 4 only here we analyze the `SLy.SB6` (*top*) and `SLy.U13` (*bottom*) configurations using the `SLy` EOS.

that the relative difference in the measured  $m = 2$  Fourier modes resulting from simulations using  $R = 11$  and  $R = 13$  initial data solutions against the simulation using  $R = 17$  to be essentially identical for both XCTS and QIC solutions. The growth of these differences is consistent throughout the simulation with only minor differences at later times. Using U13.17.M (green line), we ascertain that the growth and saturation of the relative difference at  $\sim 10^0$  is dominated by the evolution resolution, and the initial data resolution has minimal impact on the long-term evolution of the  $m = 2$  mode.

In the top panels of Fig. 5, we illustrate the evolution of the  $m = 2$  Fourier mode for the U13 configuration for the XCTS (left) and QIC (right) solutions. Both are consistent with behavior reported in Ref. [80] (see Fig. 7 therein) for the duration of the simulation.

#### D. Convergence of Dynamical Evolutions — Tabulated EOS

As a final demonstration of the capabilities of `FUKA` to compute initial data using a finite-temperature, tabulated equation of state, we present a convergence analysis of the dynamical evolution of the `SLy.U13` configuration using the `Einstein Toolkit`. Here we restrict our anal-

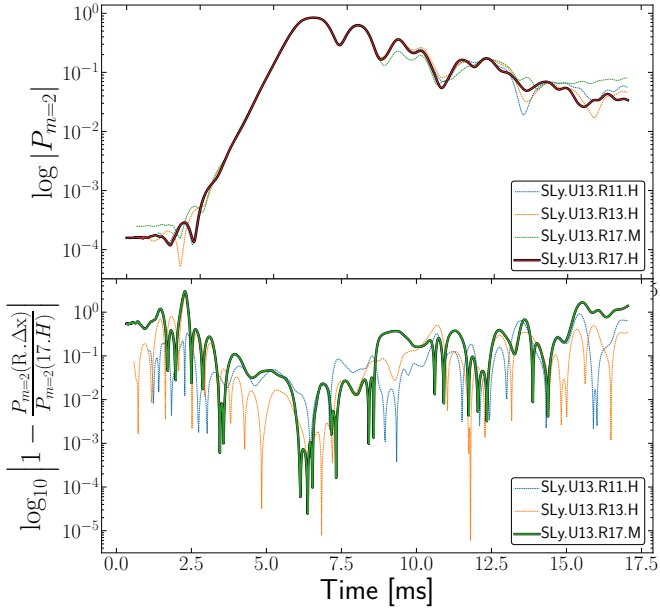


FIG. 7. Same as Fig 5 only here we focus on the **SLy.U13** configuration and the data is again aligned at the onset of the bar-mode instability.

ysis to ID produced using the XCTS solver, the **SLy** EOS and the same evolution setup as described in Sec. IV.

In Fig. 6, we illustrate the Hamiltonian constraint violations along the  $x$ -axis at  $t = 41M$  for the **SLy.SB6** (top) and **SLy.U13** (bottom) configurations. Overall we recover the expected second-order convergence (green) as predicted by the hydrodynamics evolution, though with some discrepancies at the stellar center for the U13 configuration. Additionally, we observe an overall higher magnitude of the constraint violations in the stellar interior compared to the polytropic EOS solutions. We attribute the higher constraint violations of the initial data slice (as measured in the evolution gauge) for the tabulated EOS configurations as being primarily due to the finite resolution of the **SLy** EOS and more realistic features than a polytropic EOS.

To ascertain the impact of the initial data on the long-term dynamical evolution of the **SLy.U13** configuration, we present a convergence analysis of the  $m = 2$  Fourier mode in Fig. 7. Compared to Fig. 5, we see a similar trend in the relative differences as a function of ID resolution (blue, orange lines) and evolution resolution (green line). Here we again find that the evolution resolution dominates the error growth, however, we find that the initial data resolution has a slightly more pronounced impact at the start of the simulation compared to the polytropic EOS solutions. We attribute this to the finite resolution and more rich features of the tabulated EOS as compared to the simply polytropic EOS. Thus, we observe a difference in the relaxation of the initial data slice early in the evolution, but this quickly settles and the long-term evolution is then dominated by the evolution resolution.

## VI. CONCLUSION

Precise and reliable initial data capable of accurately modeling astrophysically relevant systems is an essential component to enable accurate numerical relativity simulations with predictive power. To facilitate the study of differentially rotating neutron stars, we presented the recent extension of the **FUKA** public suite of initial data codes using two different formulations of Einstein’s field equations: the QIC and XCTS systems of equations. Both solvers leverage the accuracy of spectral methods using the **KADATH** library as well as **FUKA**’s robust framework for reliably computing initial data solutions. Furthermore, **FUKA** includes a modular EOS framework enabling the use of piecewise polytropic EOSs, tabulated EOSs in the **LORENE** format and, in the latest version of **FUKA**, 3D tabulated EOSs in the *stellar collapse* format.

To validate our solutions we demonstrated the self-convergence of each solver independently to ensure that we obtain the expected spectral convergence properties of the numerical methods. We found that spectral convergence is achieved for both solvers up to  $\tilde{N} \sim 22$  at which point the solution deteriorates due to spectral noise, a common issue with modeling steep gradients and discontinuities with spectral methods. Additionally, we compared the solutions obtained from both solvers and find excellent agreement despite considerable difference in computational and algorithmic complexity. Finally, we compared the QIC and XCTS solutions for the SB6 and U13 configurations against previously published results and find excellent agreement to three significant digits.

With confidence in the solutions computed with **FUKA**, we compared the QIC solutions against those computed using the well-established **RNS** code for a variety of differential rotation profiles and axis ratios. Overall, we find excellent agreement between the two codes, with deviations becoming pronounced for configurations on the unstable branch of the solution space. Additionally, we note that for extreme configurations ( $\hat{A} = 2.0$  and  $r_p/r_e = 0.4$ ), we were unable to compute solutions using **FUKA**. However, we leave this as an open question for future study, given the stability of solutions in this region of the parameter space, and the inconsistent trend we observed in **RNS**.

To explore the accuracy and impact of the computed ID solutions on the long-term dynamical evolution, we conducted a convergence analysis of the SB6 and U13 configurations using the **Einstein Toolkit**. Here we demonstrate the expected second-order convergence of the Hamiltonian constraint violations as well as the convergence of the  $m = 2$  Fourier mode, a key diagnostic for assessing the growth of the bar-mode instability. We found that the initial data resolution has a minimal impact on the long-term evolution of the  $m = 2$  mode, with the evolution resolution dominating the error growth and amplitude. Finally, we found that the dynamical simulations qualitatively agree with previously published results [80, 90] (see Fig. 5).

To demonstrate the ability of FUKA to compute solutions using a finite-temperature, tabulated equation of state, we computed initial data solutions using the SLy EOS and conducted a similar convergence analysis of the dynamical evolution. While we find higher constraint violations compared to the polytropic EOS solutions, we still recover the expected second-order convergence of the Hamiltonian constraint violations. We attribute the higher constraint violations of the initial data slice (as measured in the evolution gauge) for the tabulated EOS configurations primarily due to the finite resolution and rich features of the SLy EOS.

In this work, we demonstrated the accuracy and robustness for computing differentially rotating neutron star initial data using FUKA, however, there are still many avenues for future work. First, it would be essential to extend FUKA to support additional rotation profiles such as the extended KEH law [32], Uryu 8/9 laws [32], and the more recent CR laws [20]. Additionally, it would be beneficial to extend the current implementation of the XCTS solver to self-consistently support magnetic fields, which has been explored in the public LORENE [94, 95] and XNS [96] frameworks as well as the closed source COCAL code [97]. Such extensions would serve to bolster the findings in existing literature as well as enable exploration across a broader range of EOSs, rotation profiles, and fluid profiles (e.g., magnetic fields, temperature gradients). Finally, the existing codes already provide an efficient means to explore the bar-mode instability in differentially rotating neutron stars using tabulated equations of state. Such studies would provide novel insights into the impact of realistic microphysics on the growth and saturation of the bar-mode instability as well as the resulting phenomenological signatures.

## ACKNOWLEDGEMENTS

ST gratefully acknowledges support from NASA award ATP-80NSSC22K1898 and support from the University of Idaho P3-R1 Initiative. TPJ acknowledges support from NASA FINESST-80NSSC23K1437. MC acknowledges support from the European Research Council Advanced Grant ‘JETSET: Launching, propagation and emission of relativistic jets from binary mergers and across mass scales’ (grant no. 884631). This research made use of Idaho National Laboratory’s High Performance Computing systems located at the Collaborative Computing Center and supported by the Office of Nuclear Energy of the U.S. Department of Energy and the Nuclear Science User Facilities under Contract No. DE-AC07-05ID14517. Finally, this work benefited from the extensive use of the open-source packages NumPy [98], Matplotlib [99], and Kuibit [100].

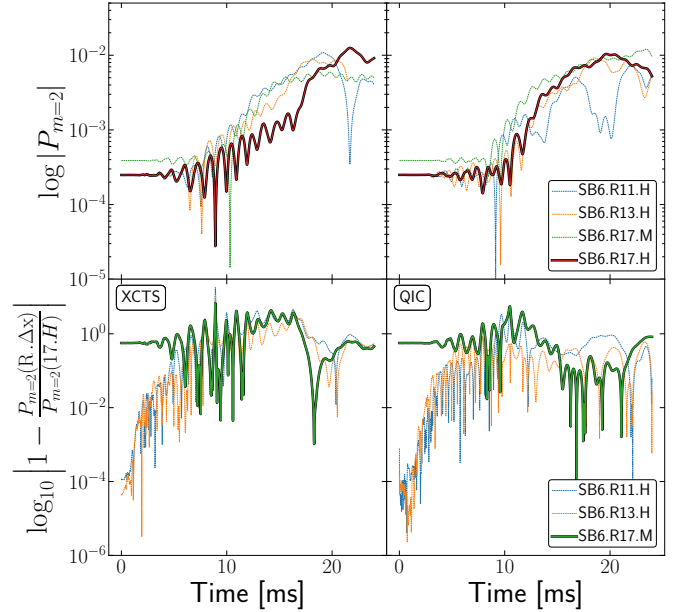


FIG. 8. Same as Fig. 5, but for the SB6 configuration.

## Appendix A: Polytropic SB6 Analysis

In this appendix, we include the convergence analysis of the  $m = 2$  Fourier mode during dynamical evolution for the SB6 configuration to assess the impact of initial data resolution  $R = \{11, 13, 17\}$  with evolution resolution  $\Delta_{Hx} = 0.32$  and  $\Delta_{Mx} = 0.4$ .

As shown in Fig. 8, we find similar behavior as that observed for the U13 configuration in Fig. 5. Specifically, during the early evolution time of  $t \lesssim 8\text{ms}$ , we find that the relative difference in the measured  $m = 2$  Fourier modes resulting from simulations using  $R = 11$  and  $R = 13$  initial data solutions against the simulation using  $R = 17$  to have a minor influence on the resulting dynamics. Unlike U13, the SB6 configuration is stable to the bar-mode instability, and thus is more sensitive to small perturbations. Therefore, we do find larger discrepancies between the very coarse  $R = 11$  initial data solution compared to the higher resolution solutions. This trend is consistent between QIC and XCTS solutions, further validating this hypothesis.

## Appendix B: Discussion on Data Alignment

In Sec. V, we presented a convergence analysis of the  $m = 2$  Fourier mode during dynamical evolution for the U13 and SLy.U13 configurations (see Figs. 5 and 7, respectively). In both cases, we aligned the datasets at the onset of the bar-mode instability to focus on the long-term behavior of the each configuration and ascertain the ID impact on the long-term behavior of the system.

To elaborate on this choice, we provide in Figs. 9 and 10 the same data presented in Figs. 5 and 7, respectively,

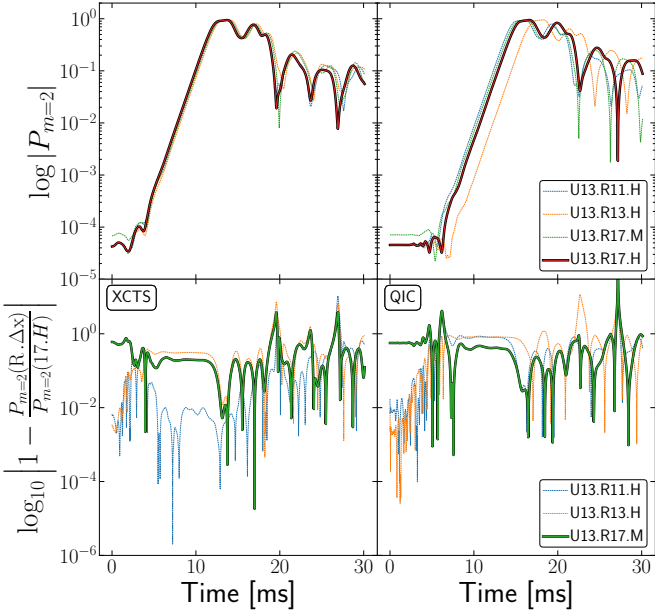


FIG. 9. Same as Fig 5 only the U13 data is not aligned.

only now the datasets are not aligned at the onset of the bar-mode instability. In the case of Fig. 9, we find that the transformation of the QIC solution from Spherical to Cartesian coordinates leads to slightly different onset time for the bar-mode instability due to higher constraint violations near coordinate singularities. As these configurations are only marginally stable, differences in the initial perturbations lead to variations in the onset time of the instability, however, the long-term behavior is consistent for all ID resolutions.

Conversely, in the case of Fig. 10, where only the XCTS solution is considered, we find that the differences in the initial data resolution can have a pronounced impact on the onset time of the bar-mode instability. Here, the differences in the initial perturbations are largely attributed to the finite resolution and more rich features of the tabulated EOS as compared to the simply polytropic EOS.

With these observations in mind, we chose to align the datasets at the onset of the bar-mode instability in order to focus on the long-term impact the ID resolution has on the system rather than on the initial perturbations that seed the instability.

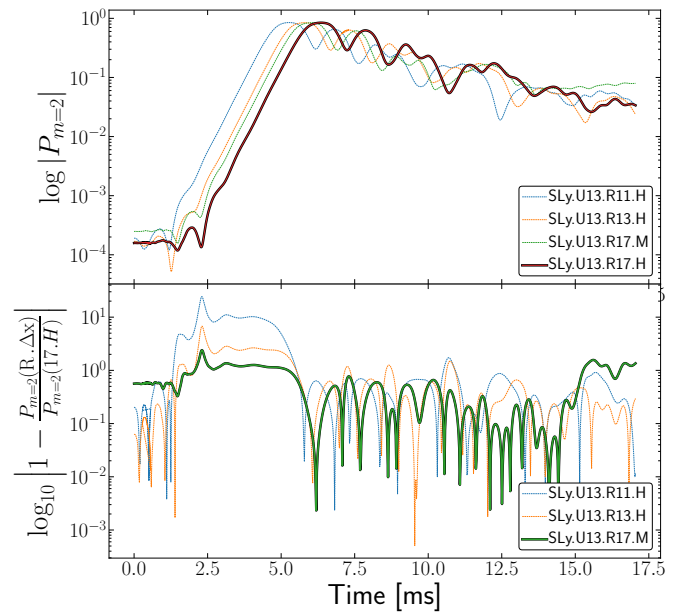


FIG. 10. Same as Fig 7 only the data is not aligned.

- [1] The LIGO Scientific Collaboration, the Virgo Collaboration, B. P. Abbott, R. Abbott, T. D. Abbott, F. Acernese, K. Ackley, C. aAdams, T. Adams, P. Addesso, R. X. Adhikari, V. B. Adya, and et al. (LIGO Scientific Collaboration and Virgo Collaboration), *Astrophys. J. Lett.* **848**, L12 (2017), arXiv:1710.05833 [astro-ph.HE].
- [2] B. P. Abbott *et al.* (LIGO Scientific, Virgo), *Phys. Rev. Lett.* **119**, 161101 (2017), arXiv:1710.05832 [gr-qc].
- [3] B. P. Abbott *et al.* (LIGO Scientific, Virgo), *Phys. Rev. Lett.* **121**, 161101 (2018), arXiv:1805.11581 [gr-qc].
- [4] B. P. Abbott *et al.* (LIGO Scientific, Virgo), *Phys. Rev. X* **9**, 011001 (2019), arXiv:1805.11579 [gr-qc].
- [5] C. D. Ott, A. Burrows, T. A. Thompson, E. Livne, and R. Walder, *Astrophys. J. Suppl. Ser.* **164**, 130 (2006), astro-ph/0508462.
- [6] A. Burrows, L. Dessart, E. Livne, C. D. Ott, and J. Murphy, *Astrophys. J.* **664**, 416 (2007), arXiv:astro-ph/0702539.
- [7] L. Dessart, A. Burrows, C. D. Ott, E. Livne, S. C. Yoon, and N. Langer, *Astrophys. J.* **644**, 1063 (2006), arXiv:astro-ph/0601603 [astro-ph].
- [8] E. B. Abdikamalov, C. D. Ott, L. Rezzolla, L. Dessart, H. Dimmelmeier, A. Marek, and H.-T. Janka, *Phys. Rev. D* **81**, 044012 (2010), arXiv:0910.2703 [astro-ph.HE].
- [9] M. Shibata, K. Taniguchi, and K. Uryū, *Phys. Rev. D* **68**, 084020 (2003), gr-qc/0310030.
- [10] L. Baiotti, B. Giacomazzo, and L. Rezzolla, *Phys. Rev. D* **78**, 084033 (2008), arXiv:0804.0594 [gr-qc].
- [11] L. Baiotti and L. Rezzolla, *Rept. Prog. Phys.* **80**, 096901 (2017), arXiv:1607.03540 [gr-qc].
- [12] M. Hanke, K. Takami, L. Bovard, L. Rezzolla, J. A. Font, F. Galeazzi, and H. Stöcker, *Phys. Rev. D* **96**, 043004 (2017), arXiv:1611.07152 [gr-qc].
- [13] A. Reboul-Salze, P. Barrère, K. Kiuchi, J. Guilet, R. Raynaud, S. Fujibayashi, and M. Shibata, *Astron. Astrophys.* **699**, A4 (2025), arXiv:2411.19328 [astro-ph.HE].
- [14] J. Bamber, A. Tsokaros, M. Ruiz, and S. L. Shapiro, *Phys. Rev. D* **111**, 044038 (2025), arXiv:2411.00943 [gr-qc].
- [15] P. Chawhan, M. D. Duez, F. Foucart, P. C.-K. Cheong, and N. Muhammed, arXiv (2025), arXiv:2510.14127

[astro-ph.HE].

[16] I. Rainho, J. Bamber, D. Guerra, M. Miravet-Tenés, M. Ruiz, A. Tsokaros, and S. L. Shapiro, arXiv (2025), [arXiv:2510.17511 \[astro-ph.HE\]](https://arxiv.org/abs/2510.17511).

[17] L. Rezzolla, F. K. Lamb, and S. L. Shapiro, *Astrophys. J. Lett.* **531**, L139 (2000), [astro-ph/9911188](https://arxiv.org/abs/astro-ph/9911188).

[18] M. Shibata, S. Karino, and Y. Eriguchi, *Mon. Not. R. Astron. Soc.* **334**, L27 (2002), [gr-qc/0206002](https://arxiv.org/abs/gr-qc/0206002).

[19] M. Sajjo, T. W. Baumgarte, and S. L. Shapiro, *Astrophys. J.* **595**, 352 (2003), [astro-ph/0302436](https://arxiv.org/abs/astro-ph/0302436).

[20] M. Cassing and L. Rezzolla, *Mon. Not. R. Astron. Soc.* **532**, 945 (2024), [arXiv:2405.06609 \[gr-qc\]](https://arxiv.org/abs/2405.06609).

[21] J. L. Friedman, J. R. Ipser, and R. D. Sorkin, *Astrophys. J.* **325**, 722 (1988).

[22] K. Takami, L. Rezzolla, and L. Baiotti, *Phys. Rev. Lett.* **113**, 091104 (2014), [arXiv:1403.5672 \[gr-qc\]](https://arxiv.org/abs/1403.5672).

[23] G. B. Cook, S. L. Shapiro, and S. A. Teukolsky, *Astrophys. J.* **398**, 203 (1992).

[24] J.-P. Lasota, P. Haensel, and M. A. Abramowicz, *Astrophys. J.* **456**, 300 (1996), [astro-ph/9508118](https://arxiv.org/abs/astro-ph/9508118).

[25] C. Breu and L. Rezzolla, *Mon. Not. R. Astron. Soc.* **459**, 646 (2016), [arXiv:1601.06083 \[gr-qc\]](https://arxiv.org/abs/1601.06083).

[26] C. Musolino, C. Ecker, and L. Rezzolla, *Astrophys. J.* **962**, 61 (2024), [arXiv:2307.03225 \[gr-qc\]](https://arxiv.org/abs/2307.03225).

[27] H. Komatsu, Y. Eriguchi, and I. Hachisu, *Mon. Not. R. Astron. Soc.* **239**, 153 (1989).

[28] N. Stergioulas and J. L. Friedman, *Astrophys. J.* **444**, 306 (1995), [astro-ph/9411032](https://arxiv.org/abs/astro-ph/9411032).

[29] A. G. Pili, N. Bucciantini, A. Drago, G. Pagliara, and L. Del Zanna, *Monthly Notices of the Royal Astronomical Society: Letters* **462**, L26 (2016).

[30] K. Franceschetti, L. Del Zanna, J. Soldateschi, and N. Bucciantini, *Universe* **8**, 172 (2022).

[31] LORENE, *Langage objet pour la relativité numérique, langage Objet pour la RElativité Numérique*, [www.lorene.obspm.fr](http://www.lorene.obspm.fr).

[32] K. Uryū, A. Tsokaros, L. Baiotti, F. Galeazzi, K. Taniguchi, and S. Yoshida, *Phys. Rev. D* **96**, 103011 (2017), [arXiv:1709.02643 \[astro-ph.HE\]](https://arxiv.org/abs/1709.02643).

[33] J. Goussard, P. Haensel, and J. L. Zdunik, *Astron. and Astrophys.* **330**, 1005 (1998), [arXiv:astro-ph/9711347](https://arxiv.org/abs/astro-ph/9711347).

[34] T. W. Baumgarte, S. L. Shapiro, and M. Shibata, *Astrophys. J. Lett.* **528**, L29 (2000), [astro-ph/9910565](https://arxiv.org/abs/astro-ph/9910565).

[35] M. Ansorg, D. Gondek-Rosińska, and L. Villain, *Mon. Not. R. Astron. Soc.* **396**, 2359 (2009), [arXiv:0812.3347 \[gr-qc\]](https://arxiv.org/abs/0812.3347).

[36] D. Gondek-Rosińska, I. Kowalska, L. Villain, M. Ansorg, and M. Kucaba, *Astrophys. J.* **837**, 58 (2017), [arXiv:1609.02336 \[astro-ph.HE\]](https://arxiv.org/abs/1609.02336).

[37] A. M. Studzińska, M. Kucaba, D. Gondek-Rosińska, L. Villain, and M. Ansorg, *Mon. Not. R. Astron. Soc.* **463**, 2667 (2016).

[38] G. Bozzola, N. Stergioulas, and A. Bauswein, *Mon. Not. R. Astron. Soc.* **474**, 3557 (2018), [arXiv:1709.02787 \[gr-qc\]](https://arxiv.org/abs/1709.02787).

[39] L. R. Weih, E. R. Most, and L. Rezzolla, *Mon. Not. R. Astron. Soc.* **473**, L126 (2018), [arXiv:1709.06058 \[gr-qc\]](https://arxiv.org/abs/1709.06058).

[40] E. Zhou, A. Tsokaros, K. Uryu, R. Xu, and M. Shibata, *Phys. Rev. D* **100**, 043015 (2019).

[41] P. L. Espino and V. Paschalidis, *Phys. Rev. D* **99**, 083017 (2019).

[42] G. Bozzola, P. L. Espino, C. D. Lewin, and V. Paschalidis, *European Physical Journal A* **55**, 149 (2019), [arXiv:1905.00028 \[astro-ph.HE\]](https://arxiv.org/abs/1905.00028).

[43] K. V. Staykov, D. D. Doneva, L. Heisenberg, N. Stergioulas, and S. S. Yazadjiev, *Phys. Rev. D* **108**, 024058 (2023), [arXiv:2303.07769 \[gr-qc\]](https://arxiv.org/abs/2303.07769).

[44] P. C.-K. Cheong, N. Muhammed, P. Chawhan, M. D. Duez, F. Foucart, L. E. Kidder, H. P. Pfeiffer, and M. A. Scheel, *Phys. Rev. D* **110**, 043015 (2024), [arXiv:2402.18529 \[astro-ph.HE\]](https://arxiv.org/abs/2402.18529).

[45] N. Muhammed, M. D. Duez, P. Chawhan, N. Ghadiri, L. T. Buchman, F. Foucart, P. Chi-Kit Cheong, L. E. Kidder, H. P. Pfeiffer, and M. A. Scheel, *arXiv e-prints*, [arXiv:2403.05642 \(2024\)](https://arxiv.org/abs/2403.05642), [arXiv:2403.05642 \[gr-qc\]](https://arxiv.org/abs/2403.05642).

[46] M. D. Duez, Y. T. Liu, S. L. Shapiro, M. Shibata, and B. C. Stephens, *Phys. Rev. D* **73**, 104015 (2006), [arXiv:astro-ph/0605331](https://arxiv.org/abs/astro-ph/0605331).

[47] B. Giacomazzo, L. Rezzolla, and N. Stergioulas, *Phys. Rev. D* **84**, 024022 (2011), [arXiv:1105.0122 \[gr-qc\]](https://arxiv.org/abs/1105.0122).

[48] P. L. Espino, V. Paschalidis, T. W. Baumgarte, and S. L. Shapiro, *Phys. Rev. D* **100**, 043014 (2019).

[49] A. Passamonti and N. Andersson, *Monthly Notices of the Royal Astronomical Society* **498**, 5904 (2020), <https://academic.oup.com/mnras/article-pdf/498/4/5904/33838626/staa2725.pdf>.

[50] X. Xie, I. Hawke, A. Passamonti, and N. Andersson, *Phys. Rev. D* **102**, 044040 (2020).

[51] G. Camellio, T. Dietrich, S. Rosswog, and B. Haskell, *Phys. Rev. D* **103**, 063014 (2021).

[52] H.-J. Kuan, K. Kiuchi, and M. Shibata, *Phys. Rev. Lett.* **135**, 141403 (2025), [arXiv:2411.16850 \[hep-ph\]](https://arxiv.org/abs/2411.16850).

[53] P. Grandclément, *J. Comput. Phys.* **229**, 3334 (2010), [arXiv:0909.1228 \[gr-qc\]](https://arxiv.org/abs/0909.1228).

[54] L. J. Papenfort, S. D. Tootle, P. Grandclément, E. R. Most, and L. Rezzolla, *Phys. Rev. D* **104**, 024057 (2021).

[55] fukascience, *Fuka enabled science*.

[56] M. Rizzo, R. Haas, S. R. Brandt, Z. Etienne, D. Ferguson, L. T. Sanches, B.-J. Tsao, L. Werneck, D. Boyer, G. Bozzola, C.-H. Cheng, S. Cupp, P. Diener, T. P. Jacques, L. Ji, H. Macpherson, I. Markin, E. Schnetter, W. Tichy, S. Tootle, Y. Xu, M. Zilhão, Y. Zlochower, M. Alcubierre, D. Alic, G. Allen, M. Ansorg, F. G. L. Armengol, M. Babiuc-Hamilton, L. Baiotti, W. Bender, E. Bentivegna, S. Bernuzzi, K. Bhatia, T. Bode, B. Brendal, B. Bruegmann, M. Campanelli, M. Chabanov, F. Cipolletta, G. Corvino, R. D. Pietri, A. Dima, H. Dimmelmeier, J. Doherty, R. Dooley, N. Dorband, M. Elley, Y. E. Khamra, L. Ennoggi, J. Faber, G. Ficarra, T. Font, J. Friebein, B. Giacomazzo, T. Goodale, C. Gundlach, I. Hawke, S. Hawley, I. Hinder, E. A. Huerta, S. Husa, T. Ikeda, S. Iyer, D. Johnson, A. V. Joshi, J. Kalinani, A. Kankani, W. Kastaun, T. Kellermann, A. Knapp, M. Koppitz, P. Laguna, G. Lanferman, P. Lasky, F. Löffler, J. Masso, L. Menger, A. Merzky, J. M. Miller, M. Miller, P. Moesta, P. Montero, B. Mundim, P. Nelson, A. Nerozzi, S. C. Noble, C. Ott, L. J. Papenfort, R. Paruchuri, M. Pirog, D. Pollney, D. Price, D. Radice, T. Radke, C. Reisswig, L. Rezzolla, C. B. Richards, D. Rideout, M. Ripeanu, L. Sala, J. A. Schewtschenko, B. Schutz, E. Seidel, E. Seidel, J. Shalf, S. Shankar, K. Sible, U. Sperhake, N. Stergioulas, W.-M. Suen, B. Szilagyi, R. Takahashi, M. Thomas, J. Thornburg, C. Tian, M. Tobias, A. Tonita, P. Walker, M.-B. Wan, B. Wardell, H. Witek, and B. Zink, *The Einstein Toolkit* (2025).

[57] N. Deppe, W. Throwe, L. E. Kidder, N. L. Vu, K. C. Nelli, C. Armaza, M. S. Bonilla, F. Hébert, Y. Kim, P. Kumar, G. Lovelace, A. Macedo, J. Moxon, E. O’Shea, H. P. Pfeiffer, M. A. Scheel, S. A. Teukolsky, N. A. Wittek, *et al.*, [SpECTRE v2025.08.19, 10.5281/zenodo.16906840](#) (2025).

[58] I. Markin, A. Neuweiler, A. Abac, S. V. Chaurasia, M. Ujevic, M. Bulla, and T. Dietrich, [Phys. Rev. D 108, 064025 \(2023\)](#), arXiv:2304.11642 [gr-qc].

[59] H.-J. Kuan, A. T.-L. Lam, D. D. Doneva, S. S. Yazadjiev, M. Shibata, and K. Kiuchi, [Phys. Rev. D 108, 063033 \(2023\)](#), arXiv:2302.11596 [gr-qc].

[60] S. Rosswog and P. Diener, SPHINCS\_BSSN: Numerical Relativity with Particles (2025) arXiv:2404.15952 [gr-qc].

[61] C. Palenzuela *et al.*, arXiv (2025), arXiv:2510.13965 [gr-qc].

[62] T. P. Jacques, S. Cupp, L. R. Werneck, S. D. Tootle, M. C. B. Hamilton, and Z. B. Etienne, [Phys. Rev. D 112, 084044 \(2025\)](#), arXiv:2412.03659 [gr-qc].

[63] M. Corman and W. E. East, [Phys. Rev. D 110, 084065 \(2024\)](#), arXiv:2405.18496 [gr-qc].

[64] S. Cupp, L. R. Werneck, T. P. Jacques, S. Tootle, and Z. B. Etienne, arXiv e-prints , arXiv:2512.15846 (2025), arXiv:2512.15846 [gr-qc].

[65] E. Gourgoulhon, arXiv e-prints , gr-qc/0703035 (2007).

[66] T. W. Baumgarte and S. L. Shapiro, *Numerical Relativity: Solving Einstein’s Equations on the Computer* (Cambridge University Press, Cambridge, UK, 2010).

[67] E. Gourgoulhon, in *CompStar 2010: School and Workshop on Computational Tools for Compact Star Astrophysics* (2010) arXiv:1003.5015 [gr-qc].

[68] P. Grandclement, C. Somé, and E. Gourgoulhon, [Phys. Rev. D 90, 024068 \(2014\)](#), arXiv:1405.4837 [gr-qc].

[69] V. Paschalidis and N. Stergioulas, [Living Rev. Rel. 20, 7 \(2017\)](#), arXiv:1612.03050 [astro-ph.HE].

[70] A. Lichnerowicz, [J. Math. Pures et Appl. 23, 37 \(1944\)](#).

[71] J. W. York, [J. Math. Phys. 14, 456 \(1973\)](#).

[72] J. W. York, [Phys. Rev. Lett. 82, 1350 \(1999\)](#).

[73] H. P. Pfeiffer and J. W. York, [Phys. Rev. Lett. 95, 091101 \(2005\)](#).

[74] stellarcollapse, Stellar collapse.

[75] GRHayL, General relativistic hydrodynamic library, general Relativistic Hydrodynamic Library, <https://github.com/GRHayL/GRHayL>.

[76] M. Shibata, T. W. Baumgarte, and S. L. Shapiro, [Astrophys. J. 542, 453 \(2000\)](#), arXiv:astro-ph/0005378.

[77] F. Löffler, R. De Pietri, A. Feo, F. Maione, and L. Franci, [Phys. Rev. D 91, 064057 \(2015\)](#), arXiv:1411.1963 [gr-qc].

[78] A. Rashti and A. Noe, [Class. Quant. Grav. 42, 015007 \(2025\)](#), arXiv:2407.01701 [gr-qc].

[79] A. Rashti, F. M. Fabbri, B. Brügmann, S. V. Chaurasia, T. Dietrich, M. Ujevic, and W. Tichy, [Phys. Rev. D 105, 104027 \(2022\)](#).

[80] L. Baiotti, R. De Pietri, G. M. Manca, and L. Rezzolla, [Phys. Rev. D 75, 044023 \(2007\)](#), arXiv:astro-ph/0609473.

[81] E. Schnetter, S. H. Hawley, and I. Hawke, [Class. Quant. Grav. 21, 1465 \(2004\)](#), arXiv:gr-qc/0310042.

[82] Z. B. Etienne, V. Paschalidis, R. Haas, P. Mösta, and S. L. Shapiro, [Classical and Quantum Gravity 32, 175009 \(2015\)](#), arXiv:1501.07276 [astro-ph.HE].

[83] T. W. Baumgarte and S. L. Shapiro, [Phys. Rev. D 59, 024007 \(1998\)](#), arXiv:gr-qc/9810065.

[84] T. Nakamura, K. Oohara, and Y. Kojima, [Prog. Theor. Phys. Suppl. 90, 1 \(1987\)](#).

[85] M. Shibata and T. Nakamura, [Phys. Rev. D 52, 5428 \(1995\)](#).

[86] H.-O. Kreiss (1973).

[87] M. Campanelli, C. O. Lousto, P. Marronetti, and Y. Zlochower, [Phys. Rev. Lett. 96, 111101 \(2006\)](#), arXiv:gr-qc/0511048.

[88] J. G. Baker, J. Centrella, D.-I. Choi, M. Koppitz, and J. van Meter, [Phys. Rev. Lett. 96, 111102 \(2006\)](#), arXiv:gr-qc/0511103.

[89] M. Alcubierre, B. Bruegmann, P. Diener, M. Koppitz, D. Pollney, E. Seidel, and R. Takahashi, [Phys. Rev. D 67, 084023 \(2003\)](#), arXiv:gr-qc/0206072.

[90] G. M. Manca, L. Baiotti, R. DePietri, and L. Rezzolla, [Classical and Quantum Gravity 24, S171 \(2007\)](#), arXiv:0705.1826 [astro-ph].

[91] E. Chabanas, P. Bonche, P. Haensel, J. Meyer, and R. Schaeffer, [Nucl. Phys. A 635, 231 \(1998\)](#), [Erratum: Nucl.Phys.A 643, 441–441 (1998)].

[92] L. R. Werneck *et al.*, [Phys. Rev. D 107, 044037 \(2023\)](#), arXiv:2208.14487 [gr-qc].

[93] N. Stergioulas, T. A. Apostolatos, and J. A. Font, [Mon. Not. R. Astron. Soc. 352, 1089 \(2004\)](#), arXiv:astro-ph/0312648.

[94] M. Bocquet, S. Bonazzola, E. Gourgoulhon, and J. Novak, [Astron. Astrophys. 301, 757 \(1995\)](#), arXiv:gr-qc/9503044.

[95] J. Novak and E. Marcq, [Class. Quant. Grav. 20, 3051 \(2003\)](#), arXiv:gr-qc/0306010.

[96] L. Del Zanna, O. Zanotti, N. Bucciantini, and P. Londrillo, [Astron. Astrophys. 473, 11 \(2007\)](#), arXiv:0704.3206 [astro-ph].

[97] K. Uryu, S. Yoshida, E. Gourgoulhon, C. Markakis, K. Fujisawa, A. Tsokaros, K. Taniguchi, and Y. Eriguchi, [Phys. Rev. D 100, 123019 \(2019\)](#), arXiv:1906.10393 [gr-qc].

[98] C. R. Harris, K. J. Millman, S. J. van der Walt, R. Gommers, P. Virtanen, D. Cournapeau, E. Wieser, J. Taylor, S. Berg, N. J. Smith, R. Kern, M. Picus, S. Hoyer, M. H. van Kerkwijk, M. Brett, A. Haldane, J. F. del Río, M. Wiebe, P. Peterson, P. Gérard-Marchant, K. Shepard, T. Reddy, W. Weckesser, H. Abbasi, C. Gohlke, and T. E. Oliphant, [Nature 585, 357 \(2020\)](#).

[99] J. D. Hunter, [Computing in Science & Engineering 9, 90 \(2007\)](#).

[100] G. Bozzola, [J. Open Source Softw. 6, 3099 \(2021\)](#), arXiv:2104.06376 [gr-qc].